9-2020

Structural Investigation of Bacilliredoxins: Enzymes Involved in Bacillithiol Redox Metabolism

Colin McHugh
Grand Valley State University

Paul Cook
Grand Valley State University

Structural Investigation of Bacilliredoxins: Enzymes Involved in Bacillithiol Redox Metabolism

Colin McHugh and Paul Cook

Department of Chemistry

Grand Valley State University

Abstract:

Bacillithiol is an important compound involved in intracellular redox homeostasis and fosfomycin resistance mechanisms of some Gram-positive bacterial pathogens. Cellular regeneration of active bacillithiol (BSH) from a disulfide (BSSB) or mixed disulfide state (BSS-Protein) involves the bacilliredoxin enzymes BrxA/B. An X-ray crystallographic structure of apo BrxA from *Bacillus subtilis* has been previously characterized, but no BrxB or BSSB-bound Brx structure currently exists. Here we present an X-ray crystallographic structure of BrxA from the pathogen *Staphylococcus aureus* with a bacillithiol disulfide (BSSB) bound in the active site. Elucidation of this structure will help researchers to understand how BSSB binds in bacilliredoxins, and provide insight into the Brx catalytic mechanism. Functional activity of YpdA, another enzyme involved in BSH regeneration, is also investigated.

Introduction:

Low molecular weight (LMW) thiols help to maintain intracellular redox homeostasis and provide protection from oxidative and electrophilic stress, such as from reactive oxygen species (ROS) (Helmann 2011, Zuber 2009). Reactive oxygen and reactive chlorine species are produced during host immune responses to damage invading pathogens (Linzner et al. 2019).

LMW thiols can form *S*-conjugates with these toxic compounds allowing for their neutralization or removal. Gram-positive firmicutes including the pathogens *Staphylococcus aureus* and *Bacillus anthracis* produce the LMW bacillithiol (BSH) in high concentration, in contrast to glutathione, which is widespread among Gram-negative bacteria and eukaryotes (Mikheyeva 2019). BSH can also act as a cofactor of enzymes such as FosB, which requires BSH to participate in deactivation of the antibiotic fosfomycin (Roberts et al. 2013). Target selectivity and BSH-dependent fosfomycin resistance makes BSH-associated enzymes a potential focus for inhibitory drug design, in which treatment would be applied in conjunction with fosfomycin. Disruption of the BSH pathway may also increase a pathogen's vulnerability to environmental stresses and/or decrease resistance to the anti-TB drug rifamycin (Newton, Fahey and Rawat 2012).

Scheme 1- Brx-mediated debacillithiolation

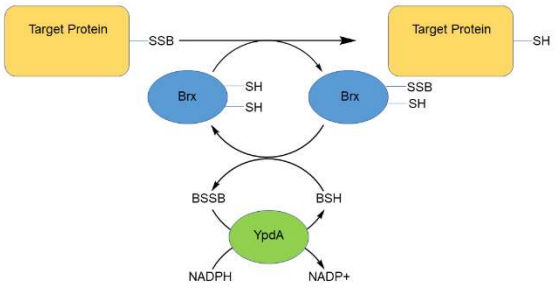

The oxidation state of bacillithiol can alternate between a free thiol, a BSSB disulfide, or a BSS-protein mixed disulfide in response to enzymatic catalysis or cellular conditions (Scheme 1). When *Staphylococcus* and *Bacillus* species are introduced to oxidative stress, BSH can be attached to protein thiol groups to protect them (Linzner et al. 2019, Mikheyeva 2019). Currently unknown enzymes perform a transferase reaction with BSH to form a BSS-protein disulfide, ensuring protection of the protein from oxidative damage. This protein must be subsequently debacillithiolated to further the BSH regeneration pathway and reestablish catalytic activity. It has been proposed that the bacilliredoxin enzymes BrxA and BrxB carry out this BSH transferase reaction, resulting in a BSS-Brx mixed disulfide and/or BSSB disulfide (Loi, Rossius and Antelmann 2015, Posada et

al. 2014). BSH regeneration is continued by other enzymes, including NADPH-dependent YpdA which is proposed to function as a bacillithiol disulfide reductase on BSS-Brx or BSSB to produce the free thiol (Mikheyeva 2019). Further investigation is needed to determine the role of YpdA in the BSH pathway.

The X-ray crystallographic structure of apo BrxA from *B. subtilis* has been previously characterized (Figure 1), but no structure of a bacillithiol-bound Brx exists. The available BrxA structure displays an unusual CXC catalytic motif in contrast to the CXXC motif common among other thioredoxins. The CXC residues are key to the disulfide-exchange reactions characteristic of bacilliredoxins, but it is currently unknown which cysteine participates in the mixed disulfide with bacillithiol (Derewenda et al. 2009). Structural characterization of the Brx enzymes from *S. aureus* and *B. subtilis* under oxidative conditions is necessary to understand how and where bacillithiol binding occurs, as well as the mechanism of Brx activity. Here we describe the 1.4 Å X-ray crystallographic structure of BrxA from *S. aureus* with a bacillithiol disulfide bound in the active site.

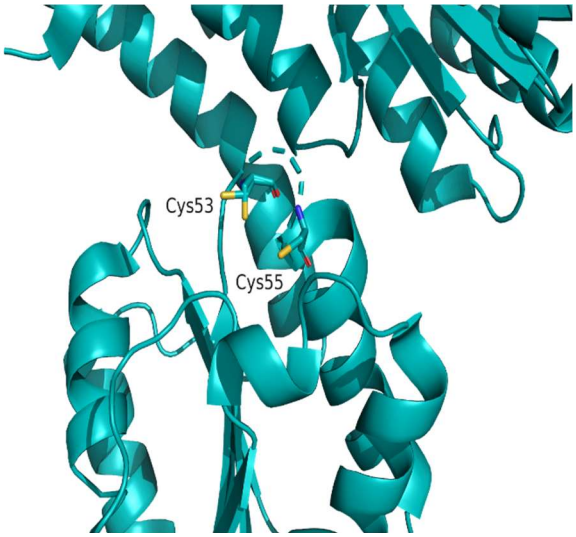

Figure 1: Apo BrxA structure with CXC cysteines labeled

Materials and Methods

Expression and purification

Transformation of chemically competent *E. coli* BL-21(DE3) cells was accomplished using a pET28 expression vector encoding for an N-terminal hexahistidine tag and the bacilliredoxin gene. Transformed cells were plated on LB media containing 25 μg/mL kanamycin to allow for selection, and subsequently grown in liquid media until reaching an optical density of 0.97 for BrxA from *S. aureus*, 1.004 from *B. subtilis*, and 0.845, 0.66, for BrxB from *B. subtilis*. Bacilliredoxin production was induced by the addition of IPTG to a final concentration of 0.5 mM and the cultures agitated by shaking at 200 rpm in 16 °C for ~18-24 hours. Cells were harvested via centrifugation, stored in -20 °C, resuspended in a buffered solution, lysed enzymatically and sonicated to produce a crude lysate. Bacilliredoxin purification was accomplished through nickel affinity chromatography, subsequent rTEV cleavage, and dialysis against 20 mM HEPES (pH 7.5) and 50 mM NaCl. Enzyme purity was assessed via SDS-PAGE analysis.

Crystallization, data collection, and processing

Bacilliredoxin crystallization trials were prepared using the hanging drop method of vapor diffusion. Crystallization was attempted with BrxA from *B. subtilis* in apo state and supplemented with 1 mM BSSB, and in BrxA from *S. aureus* in apo state and supplemented with either 1 mM BSSB, cysteine, N-acetylglucosamine (GlcNac), tris(2-carboxyethyl)phosphine hydrochloride (TCEP), or dithiothreitol (DTT). X-ray diffraction experiments were performed via the Life Sciences Collaborative Access Team at Argonne National Laboratory. A data set was collected from suitable BrxA *S. aureus* crystals grown in a 0.2 M Ammonium phosphate monobasic, 20% w/v Polyethylene glycol 3,350 well solution. The data were processed with autoPROC (Vonrhein et al. 2011). The structure of BrxA was solved via molecular replacement with Phaser using BrxA from B. subtilis as the search probe (McCoy et al. 2007). The model was

built in Coot (Emsley et al. 2010) and refined in Refmac (Murshudov et al. 2011). All figures were generated in PyMOL (PyMOL).

Initial kinetics assay of YpdA

Analysis of YpdA kinetic activity was measured using a Cary UV-Vis spectrophotometer at an absorbance of 340 nm, and a 50 mM HEPES (pH 8.0) 50 mM NaCl buffered solution containing either 180 μM NADPH, 12.5 μM $FADH_2$, 40 μM BSSB with varied YpdA concentration, or, 12.5 μM YpdA, 180 μM NADPH, 12.5 μM $FADH_2$, with varied BSSB concentration.

Results and Discussion

Expression and purification of BrxA and BrxB

Analysis via SDS-PAGE indicated significant impurities in the expression of both BrxA and BrxB obtained from *B. subtilis* (Figures 2, 3, 4). The purity of BrxA *S. aureus* was assessed (Figure 5), and protein fractions numbered 12-25 were deemed pure, pooled, and stored.

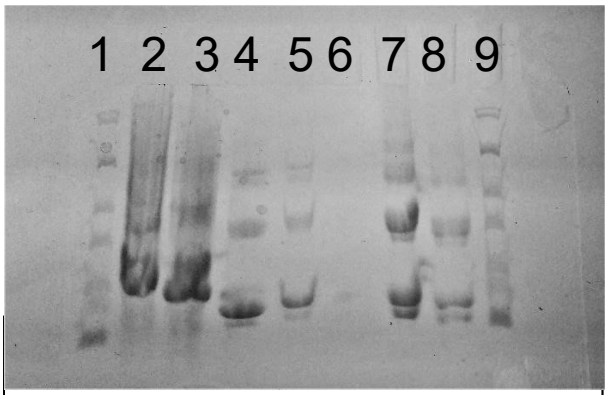

Figure 2- SDS PAGE analysis of impure BrxA *Bs* from transformed BL-21 cells: Lane 1 and 9 include a protein ladder. Lane 2 the crude lysate and lane 3 the clarified lysate. Lane 4 the rTEV digest including rTEV, lane 5 without rTEV. Lane 6 is empty. Lane 7 and 8 include 20μL and 5 μL of the purified enzyme.

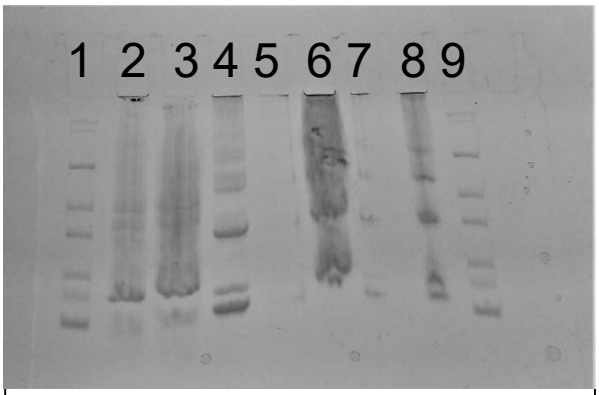

Figure 3- SDS PAGE analysis of impure BrxB *Bs* from transformed BL-21 cells: Lane 1 and 9 include a protein ladder. Lane 2 the crude lysate and lane 3 the clarified lysate. Lane 4 rTEV digest. Lanes 5 and 7 are empty. Lanes 6 and 8 include 20μL and 5μL of the purified enzyme.

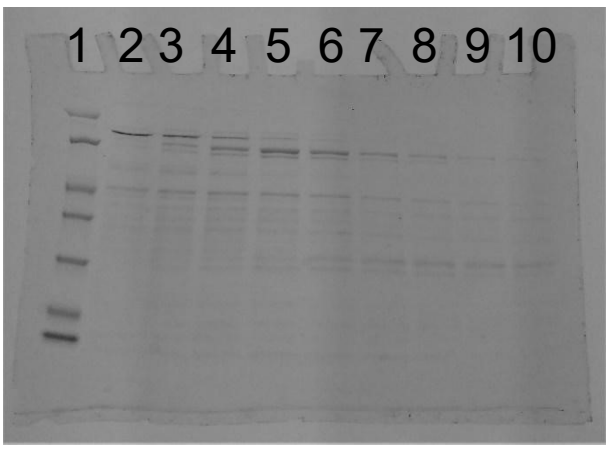

Figure 4- SDS PAGE analysis of impure BrxB *Bs* Ni affinity chromatography fractions from transformed BL-21 cells: Lane 1 includes a protein ladder. Lanes 2-4 include purified fractions 8-10. Lane 5 includes fraction 12, lane 6 fraction 14, and lane 7 fraction 16. Lanes 8-10 include fractions 17-19.

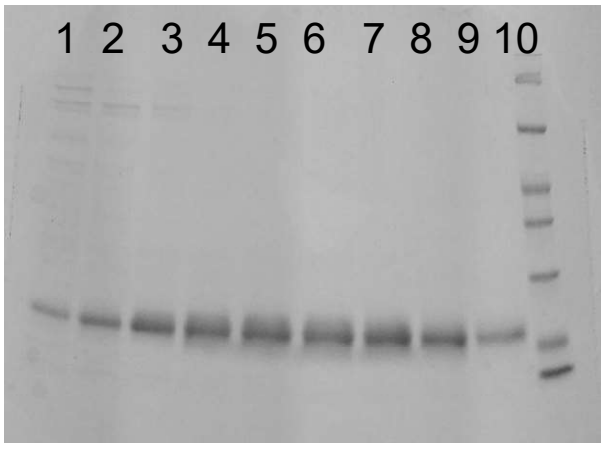

Figure 5- SDS PAGE analysis of pure BrxA *Sa* Ni affinity chromatography fractions from transformed BL-21 cells: Lane 10 includes a protein ladder. Lane 1 includes purified fraction 8, lane 2 fraction 10, lane 3 fraction 12, lane 4 fraction 14, lane 5 fraction 16, lane 6 fraction 18, lane 7 fraction 20, lane 8 fraction 22, and lane 9 fraction 25.

YpdA Kinetics:

Preliminary results of YpdA kinetics display a linear slope in absorbance over time, indicating enzymatic activity when accounting for background oxidation of NADPH (Figure 6). A somewhat linear relationship in initial velocity was observed with increasing YpdA concentration, resulting in an R^2 value of 0.93 (Graph 1). Comparison of initial velocity with increasing

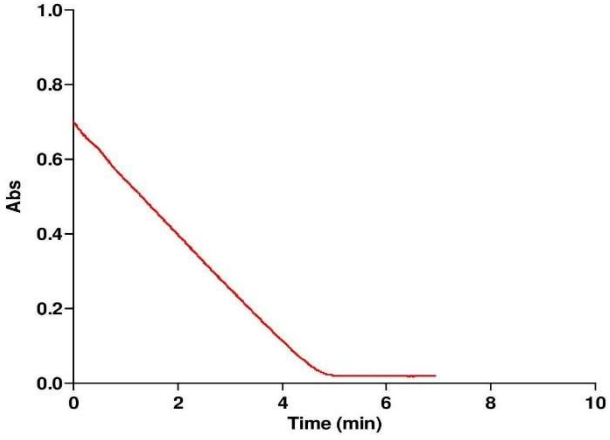

Figure 6: Assay validation of YpdA with 40µM BSSB

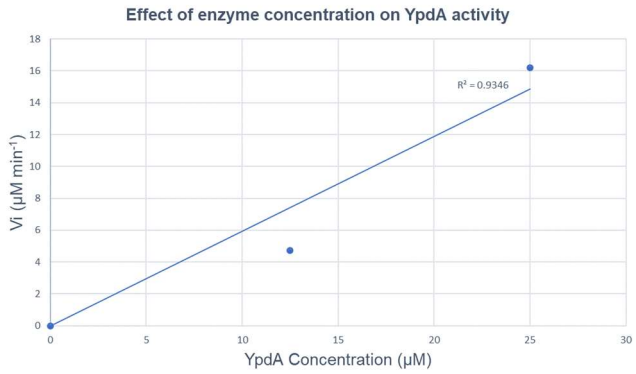

Graph 1: Analysis of initial YpdA activity with increasing enzyme concentration.

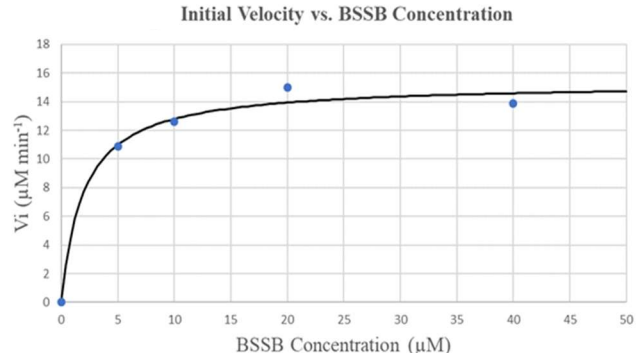

Graph 2: Analysis of initial YpdA activity with increasing BSSB concentration.

BSSB concentration suggests the possibility of typical enzyme-substrate hyperbolic behavior (Graph 2), however, the assay was not completed under steady state conditions due to a very high enzyme concentration. These results suggest that YpdA may function as a reductase of BSSB at a very slow catalytic rate, but the role and inclusion of YpdA in the bacillithiol pathway remains questionable. Based on these results, YpdA may perform this reaction in the cell, however, the intracellular enzyme concentration would have to be very high. It is also possible that the purification and expression process used to obtain YpdA resulted in an enzyme with lower activity than would be observed intracellularly, or other factors could be missing from the experimental design. Further investigation under steady state conditions is required to accurately assess YpdA activity.

Structure of BrxA from S. aureus

A data set was collected from BrxA *S. aureus* with BSSB bound in the active site. A 1.37 Å structure was solved and the asymmetric unit was shown to contain one polypeptide. Crystallization and refinement statistics are displayed in Table 1. Ramachandran statistics are good, indicating that 97.5 % of residues fall within favored regions (Table 1). We presume the formation of a biological homodimer is likely in BrxA *S. aureus* (Figure 7), as is observed in other thioredoxins, and as predicted by PDBePISA (Krissinel and Henrick 2007). The active site region is present near the protein's surface, allowing for ease of interaction between BrxA and other proteins during bacillithiol transfer.

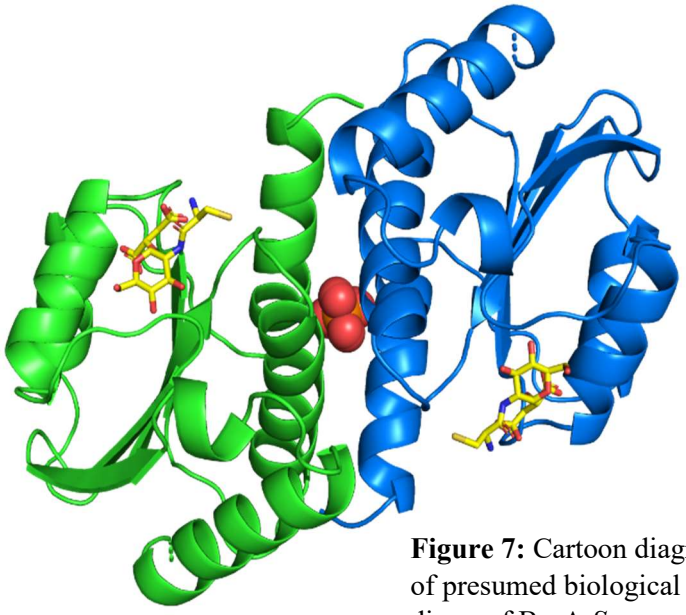

Figure 7: Cartoon diagram of presumed biological dimer of BrxA *S. aureus* colored by chain.

Table 1: Crystallization and refinement statistics from BrxA *S. aureus.*

[a]Values in parentheses are for the highest resolution bin. [b]Heteroatoms include 77 water molecules, 1 BSSB, and 1 PO4- molecule.

Data collection statistics	
Space Group	$P4_12_12$
Unit cell dimensions (Å)	a = b = 85.7, c = 42.1
Resolution Limits (Å)	42.9–1.37(1.47–1.37)[a]
Number of Independent Reflections	23743 (1188)
Completeness (%)	94.7 (64.8)
Redundancy	23.6 (15.5)
Avg (I / σ(I))	27.7 (1.3)
R_{merge}	0.053 (1.683)
R_{pim}	0.015 (0.595)
$CC_{1/2}$	.999 (.588)

Refinement statistics	
$R_{overall}$ (%)	19.9
R_{work} (%)	19.9
R_{free} (%)	21.5
No. Protein Atoms	1107
No. Hetero-Atoms	107[b]
Average B values	
Protein Atoms (Å^2)	26.0
Ligand Atoms (Å^2)	34.3
Solvent (Å^2)	30.3
Weighted root-mean-square deviations from ideality	
Bond Lengths (Å)	0.013
Bond Angles (deg)	1.859
General Planes (Å)	0.009
Ramachandran statistics	
Favored (%)	97.5
Allowed (%)	1.67
Outliers (%)	0.83

Active site

The BrxA *S. aureus* active site contains a well-defined bacillithiol covalently bound to Cys54. This structure is the first to reveal that the N-terminal cysteine in the CXC catalytic motif is responsible for bacillithiol binding (Figure 8). Arg121 lies in near proximity to the bound substrate and likely functions in stabilization of the thiolate formed during the bacillithiol transferase reaction.

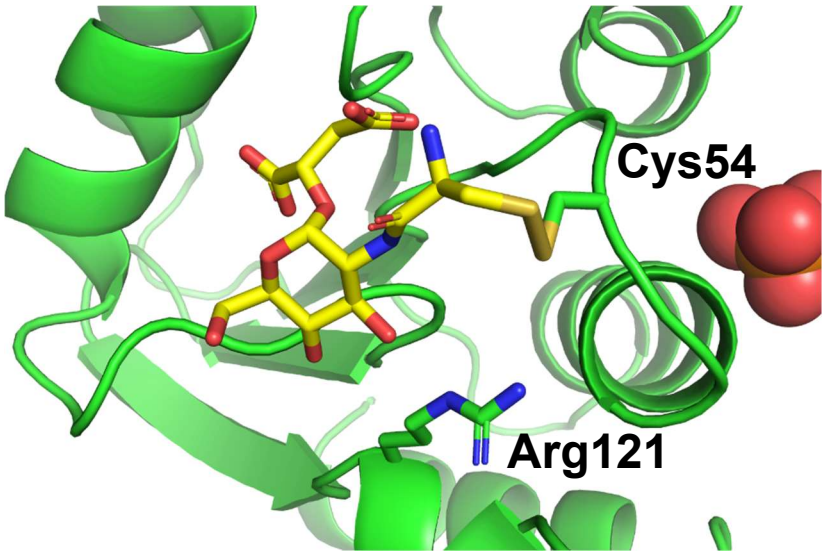

Figure 8: Diagram of BrxA *S. aureus* active site with a bacillithiol bound. Residues involved in substrate interaction are labeled.

Comparison with BrxA B. subtilis

Comparison of the structure of BrxA *S. aureus* presented here, with that of previously characterized apo BrxA *B. subtilis*, reveals a similar monomeric conformation, with only slight differences (Figure 9). The binding of bacillithiol in the active site by Cys54 observed in BrxA *S. aureus* reveals that Cys53 in BrxA *B. subtilis*

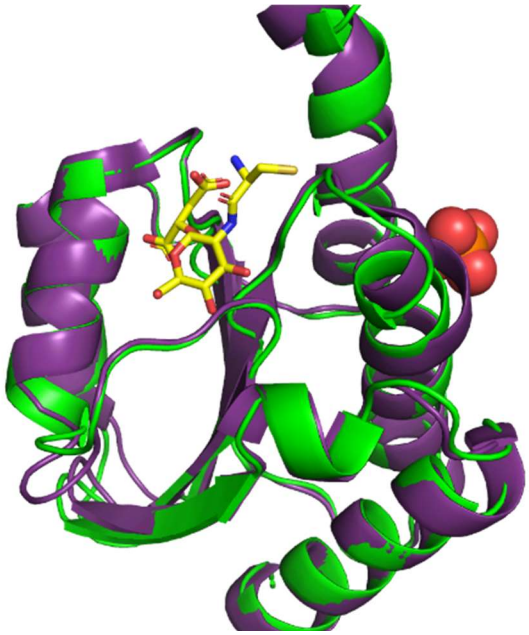

Figure 9: Cartoon diagram displaying the overlay of monomers from BrxA *S. aureus* (green) with BrxA *B. subtilis* (purple).

is likely responsible for substrate binding in a similar manner. The residues are located near the same position in the active site, at the N-terminal end of the CXC catalytic motif. Arg121 is also shown to be present in both enzymes, likely functioning in thiolate stabilization (Figure 10). Overall, these results suggest a high degree of similarity in BrxA between these organisms.

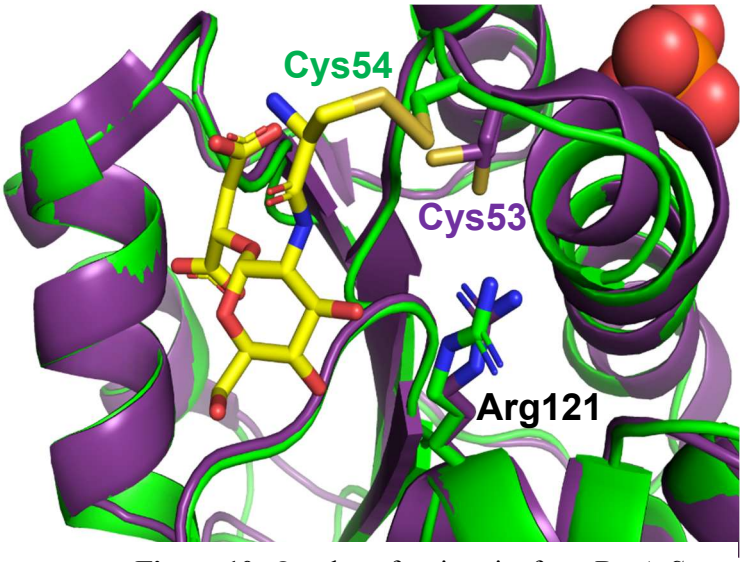

Figure 10: Overlay of active site from BrxA *S. aureus* (green) with BrxA *B. subtilis* (purple). Residues involved in substrate interaction are labeled.

Conclusion

The X-ray crystallographic structure of BrxA presented here is the first ever X-ray crystallographic structure of a Brx enzyme bound in a BSS-Brx mixed disulfide, and the first structure of BrxA from *S. aureus*. Elucidation of this structure provides insight into the exact manner of bacillithiol binding, and the mechanism of bacilliredoxin activity. Novel discoveries into the BSH regeneration pathway in pathogenic firmicutes such as *S. aureus* and *B. anthracis* can aid in combatting bacterial resistance to antibiotics such as fosfomycin, as well as providing a potential for novel drug therapies.

References:

Derewenda, U., T. Boczek, K. L. Gorres, M. Yu, L. W. Hung, D. Cooper, A. Joachimiak, R. T. Raines & Z. S. Derewenda (2009) Structure and function of Bacillus subtilis YphP, a prokaryotic disulfide isomerase with a CXC catalytic motif. *Biochemistry,* 48**,** 8664-71.

Helmann, J. D. (2011) Bacillithiol, a new player in bacterial redox homeostasis. *Antioxid Redox Signal,* 15**,** 123-33.

Linzner, N., V. V. Loi, V. N. Fritsch, Q. N. Tung, S. Stenzel, M. Wirtz, R. Hell, C. J. Hamilton, K. Tedin, M. Fulde & H. Antelmann (2019) Uses the Bacilliredoxin (BrxAB)/Bacillithiol Disulfide Reductase (YpdA) Redox Pathway to Defend Against Oxidative Stress Under Infections. *Front Microbiol,* 10**,** 1355.

Loi, V. V., M. Rossius & H. Antelmann (2015) Redox regulation by reversible protein S-thiolation in bacteria. *Front Microbiol,* 6**,** 187.

Mikheyeva, I. V., et al (2019). YpdA, a putative bacillithiol disulfide reductase, contributes to cellular redox homeostasis and virulence in *Staphylococcus aureus*. 1039-1056. *Molecular Microbiology*.

Newton, G. L., R. C. Fahey & M. Rawat (2012) Detoxification of toxins by bacillithiol in Staphylococcus aureus. *Microbiology,* 158**,** 1117-1126.

Posada, A. C., S. L. Kolar, R. G. Dusi, P. Francois, A. A. Roberts, C. J. Hamilton, G. Y. Liu & A. Cheung (2014) Importance of bacillithiol in the oxidative stress response of Staphylococcus aureus. *Infect Immun,* 82**,** 316-32.

Roberts, A. A., S. V. Sharma, A. W. Strankman, S. R. Duran, M. Rawat & C. J. Hamilton (2013) Mechanistic studies of FosB: a divalent-metal-dependent bacillithiol-S-transferase that mediates fosfomycin resistance in Staphylococcus aureus. *Biochem J,* 451**,** 69-79.

Zuber, P. (2009) Management of oxidative stress in Bacillus. *Annu Rev Microbiol,* 63**,** 575-97.

Emsley, P., B. Lohkamp, W. G. Scott & K. Cowtan (2010) Features and development of Coot. Acta Crystallogr D Biol Crystallogr, 66, 486-501.

Krissinel, E. & K. Henrick (2007) Inference of macromolecular assemblies from crystalline state. J Mol Biol, 372, 774-97.

McCoy, A. J., R. W. Grosse-Kunstleve, P. D. Adams, M. D. Winn, L. C. Storoni & R. J. Read (2007) Phaser crystallographic software. J Appl Crystallogr, 40, 658-674.

Murshudov, G. N., P. Skubák, A. A. Lebedev, N. S. Pannu, R. A. Steiner, R. A. Nicholls, M. D. Winn, F. Long & A. A. Vagin (2011) REFMAC5 for the refinement of macromolecular crystal structures. Acta Crystallogr D Biol Crystallogr, 67, 355-67.

Vonrhein, C., C. Flensburg, P. Keller, A. Sharff, O. Smart, W. Paciorek, T. Womack & G. Bricogne. 2011. Data processing and analysis with the autoPROC toolbox. 293-302. Acta Crystallographica.

The PyMOL Molecular Graphics System, version 1.5.0.4 (2012). Schrodinger, LLC, Portland, OR.

Appendix

RMD Manuscript submitted to the journal *Proteins*:

X-ray crystallographic structure of RMD from *Pseudomonas aeruginosa*, the NAD(P)H-dependent reductase involved in GDP-D-rhamnose production

Benjamin E. Nicholson,[‡] Colin S. McHugh,[‡] and Paul D. Cook,[‡,*]

[‡]Department of Chemistry, Grand Valley State University, Allendale, Michigan, 49401

[*]To whom correspondence should be addressed:

Email: cookp@gvsu.edu

Phone: 616-331-8631

Fax: 616-331-3230

Running title: RMD structure

ACKNOWLEDGEMENTS

This research used resources of the Advanced Photon Source, a U.S. Department of Energy (DOE) Office of Science User Facility operated for the DOE Office of Science by Argonne National Laboratory under Contract No. DE-AC02-06CH11357. Use of the LS-CAT Sector 21 was supported by the Michigan Economic Development Corporation and the Michigan Technology Tri-Corridor (Grant 085P1000817).

ABSTRACT

A unique O-antigen known as the A-band is present in the lipopolysaccharide of *Pseudomonas aeruginosa* and consists of the deoxy sugar D-rhamnose. GDP-linked

D-rhamnose production involves a two-enzyme pathway, including the short-chain dehydrogenase/reductase GDP-4-keto-6-deoxymannose-4-reductase, also known as RMD. Here we describe the first ever X-ray crystallographic structure of RMD from *P. aeruginosa*, which is also the first RMD structure that displays a well-ordered NADPH cofactor. Elucidation of this structure provides insight into the catalytic mechanism of RMD and the D-rhamnose biosynthetic pathway.

Keywords: Lipopolysaccharide, *Pseudomonas*, X-ray crystallography, O-antigen, short-chain dehydrogenase/reductase

INTRODUCTION

Gram-negative bacteria display on their surface a membrane-associated lipopolysaccharide (LPS), which functions in stabilization, defense from antimicrobials, communication, and participation in host immune response.[1, 2] The distal portion of the LPS contains a repeating sugar structure known as the O-antigen. Compositional variation among O-antigens can contribute to a pathogen's virulence. This effect is displayed in the common nosocomial pathogen *Pseudomonas aeruginosa*, in which an O-antigen termed A-band is composed of the deoxy sugar D-rhamnose.[3] O-antigen biosynthesis utilizes nucleotide-linked sugars, and in *P. aeruginosa*, D-rhamnose biosynthesis begins with GDP-D-mannose. Via GDP-mannose-4,6-dehydratase (GMD), GDP-mannose undergoes dehydration to produce GDP-4-keto-6-deoxymannose (Scheme S1).[4] The keto group is then reduced in a stereospecific manner by GDP-4-keto-6-deoxymannose-4-reductase (RMD) to produce GDP-D-rhamnose. RMD utilizes either NADPH or NADH with no significant preference.[5]

GMD has been well-characterized. An X-ray crystallographic structure was determined for RMD from *Aneurinibacillus thermoaerophilus* (*At*RMD).[3] However, that structure contains a partially disordered NADPH cofactor that lacks the redox-active nicotinamide ring. Here we describe the 1.9 Å resolution crystal structure of NADPH-bound RMD from *P. aeruginosa* (*Pa*RMD), the first ever RMD structure from this organism. The nicotinamide ring of the NADPH is clearly defined and provides insight into the catalytic mechanism of RMD.

2. MATERIALS AND METHODS

*Pa*RMD was expressed recombinantly in *Escherichia coli* and purified by nickel affinity chromatography. Crystals of RMD with an N-terminal hexahistidine tag were grown via vapor diffusion. The crystals were frozen in liquid nitrogen and X-ray data were collected at the Life Sciences Collaborative Access Team at Argonne National Laboratory. The structure was solved via molecular replacement using *At*RMD (PDB ID 2PK3) as the search model.[3] Data collection and refinement statistics are displayed in Table 1. Additional experimental details can be found in the Supporting Information.

3. RESULTS AND DISCUSSION

3.1 Overall structure

The RMD crystals from this experiment contained four polypeptide chains in the asymmetric unit. Ramachandran statistics determined from the PDB Validation Report indicate 97.9 % of residues are present in favored regions, with no outliers (Table 1). The A and B chains are well ordered overall, but the C and D chains contain several surface loops that are partially disordered. Nonetheless, we were able to model most of each polypeptide chain, with the exception of the termini and a chain break in a loop roughly between Gln154 and Gln164 in all four chains. This loop is located at the surface of the protein and is away from the active site region. The RMD monomer contains a Rossman fold core as expected in short-chain dehydrogenase/reductase (SDR) family enzymes (Figure 1A, 1B and S1). Examination of the unit cell contents and analysis via PDBePISA[6] support the formation of the dimer commonly seen among SDR enzymes in which a four-helix bundle forms an interface between chains A and B (Figure S1B, Supporting Information). Chains C and D form a second copy of this biological dimer.

3.2 Active site

RMD binds NAD(P)H in the N-terminal domain and GDP-4-keto-6-deoxymannose in the C-terminal domain. Electron density corresponding to NADPH was apparent in the active site in all four chains (Figure S2A). Given that the electron density map is strongest for the ligand in chain B, the remainder of this analysis will refer to it. Several side chain and main chain groups interact with NADPH (Figure 1C). Many of these interactions are identical to those found in *At*RMD, including stabilization of the NADPH phosphoryl groups via interactions with the δ^+ end of the α1 helix. The nicotinamide ring in our structure is clearly ordered, and its amide group forms a hydrogen bond with the side chain of Gln166. The catalytic triad residues Ser105, Tyr131, and Lys135 are all situated near the B-face of the nicotinamide ring. Ser105 makes no interactions with NADPH, but Tyr131 and Lys135 hydrogen bond to the NADPH ribose hydroxyl groups. Several peaks in the F_o - F_c map were present within the GDP-4-keto-6-deoxymannose binding site that belonged to a low occupancy NADPH molecule bound in a non-productive manner. The density was strong enough to model this additional NADPH into chain D and pyrophosphate into Chain B, but we left the density unmodeled in chains A and C.

3.3 Mechanism

The *At*RMD structure contains GDP-mannose bound within the GDP-4-keto-6-deoxymannose binding site.[3] Therefore, the superposition of the *At*RMD and *Pa*RMD structures provides a good model for the product-bound state of the enzyme (Figure 1D and S3). The superposition places the 4-carbon of GDP-mannose near the 4-carbon of the nicotinamide ring

and the 4-hydroxyl group of GDP-mannose near Ser105 and Tyr131. This arrangement of groups supports a mechanism in which Tyr131 protonates the keto oxygen while the hydride is transferred from NAD(P)H (Scheme S2).[7] Ser105 serves to stabilize the forming hydroxyl group, whereas Lys135 lowers the pK_a of Tyr131 and participates in a proton relay assisted by the 2-hydroxyl group of the ribose.

The structure of RMD presented here provides insight into the biosynthesis of D-rhamnose, a deoxy sugar that forms a critical component within the LPS of the pathogenic bacterium *P. aeruginosa*. Furthermore, a thorough understanding of deoxysugar biosynthesis pathways can aid in the production of novel sugars.[8] Such sugars can be utilized in glycodiversification processes such as attachment to macrolide antibiotic scaffolds to make novel therapeutic compounds.[9]

REFERENCES

1. Lerouge I, Vanderleyden J. O-antigen structural variation: mechanisms and possible roles in animal/plant-microbe interactions. *FEMS Microbiol Rev*. Mar 2002;26(1):17-47.

2. Samuel G, Reeves P. Biosynthesis of O-antigens: genes and pathways involved in nucleotide sugar precursor synthesis and O-antigen assembly. *Carbohydr Res*. Nov 2003;338(23):2503-19.

3. King JD, Poon KKH, Webb NA, *et al*. The structural basis for catalytic function of GMD and RMD, two closely related enzymes from the GDP-D-rhamnose biosynthesis pathway. *FEBS J*. May 2009;276(10):2686-2700.

4. Mäki M, Järvinen N, Räbinä J, *et al*. Functional expression of *Pseudomonas aeruginosa* GDP-4-keto-6-deoxy-D-mannose reductase which synthesizes GDP-rhamnose. *Eur J Biochem*. Jan 2002;269(2):593-601.

5. Kneidinger B, Graninger M, Adam G, *et al*. Identification of two GDP-6-deoxy- D-lyxo-4-hexulose reductases synthesizing GDP- D-rhamnose in *Aneurinibacillus thermoaerophilus* L420-91T. *J Biol Chem*. Feb 2001;276(8):5577-83.

6. Krissinel E, Henrick K. Inference of macromolecular assemblies from crystalline state. *J Mol Biol*. Sep 2007;372(3):774-97.

7. Filling C, Berndt KD, Benach J, et al. Critical residues for structure and catalysis in short-chain dehydrogenases/reductases. *J Biol Chem*. Jul 2002;277(28):25677-84.

8. Cook PD, Holden HM. GDP-perosamine synthase: structural analysis and production of a novel trideoxysugar. *Biochemistry*. Mar 2008;47(9):2833-40.

9. Thibodeaux CJ, Melançon CE, Liu HW. Unusual sugar biosynthesis and natural product glycodiversification. *Nature*. Apr 2007;446(7139):1008-16.

10. The PyMOL Molecular Graphics System, version 1.5.0.4 (2012). Schrodinger, LLC, Portland, OR.

Table 1: X-ray Data Collection and Refinement Statistics

	RMD (6X3B)
Data collection statistics	
Space Group	$P2_1$
Unit cell dimensions (Å)	a = 97.7, b =54.1, c =137.9, β = 107.7°
Resolution Limits (Å)	34.03–1.91(1.94–1.91)[a]
Number of Independent Reflections	105890 (5178)
Completeness (%)	99.1 (98.5)
Redundancy	5.0 (5.0)
Avg (I / σ(I))	8.5 (1.6)
R_{merge}	0.090 (0.813)
R_{pim}	0.070 (0.622)
$CC_{1/2}$	0.997 (0.666)
Refinement statistics	
$R_{overall}$ (%)	18.9
R_{work} (%)	18.7
R_{free} (%)	22.4
No. Protein Atoms	9141[b]
No. Hetero-Atoms	778[c]
Average B values	
Protein Atoms (Å^2)	35.3
Ligand Atoms (Å^2)	35.5
Solvent (Å^2)	35.6
Weighted root-mean-square deviations from ideality	
Bond Lengths (Å)	0.007
Bond Angles (deg)	0.85
General Planes (Å)	0.005
Ramachandran statistics	
Favored (%)	97.9

Allowed (%)	2.1
Outliers (%)	0

[a]Values in parentheses are for the highest resolution bin.

[b]Four polypeptides (two biological dimers) are present in the asymmetric unit.

[c]Heteroatoms include 525 water molecules, five NADPH molecules, one pyrophosphate ion, and one nitrate ion.

FIGURE LEGENDS

Figure 1. The structure of RMD. (A) Cartoon diagram of the RMD monomer with NADPH shown in spheres. The binding site for the substrate GDP-4-keto-6-deoxymannose in the C-terminal domain is indicated. All macromolecular graphics were generated in PyMOL.[10] **(B)** Amino acid sequence of RMD. The secondary structural elements labelled within the RMD structure are shown in blue above the sequence. The numbers in black below the sequence indicate the residue number at the beginning of an element. **(C)** Close-up view of the RMD active site. Polar interactions within 3.2 Å of the NADPH are shown with dashed lines. The adenine base is indicated with an "A" and the nicotinamide group is indicated with an "N" for clarity. **(D)** Superposition of RMD structures. The *Pa*RMD structure is shown with green carbons, whereas the *At*RMD structure is shown with tan carbons and labels with asterisks. Carbon #4 in both NADPH and GDP-mannose are labelled. The dashed lines indicate hydrogen bonding interactions relevant to the catalytic mechanism.

FIGURE

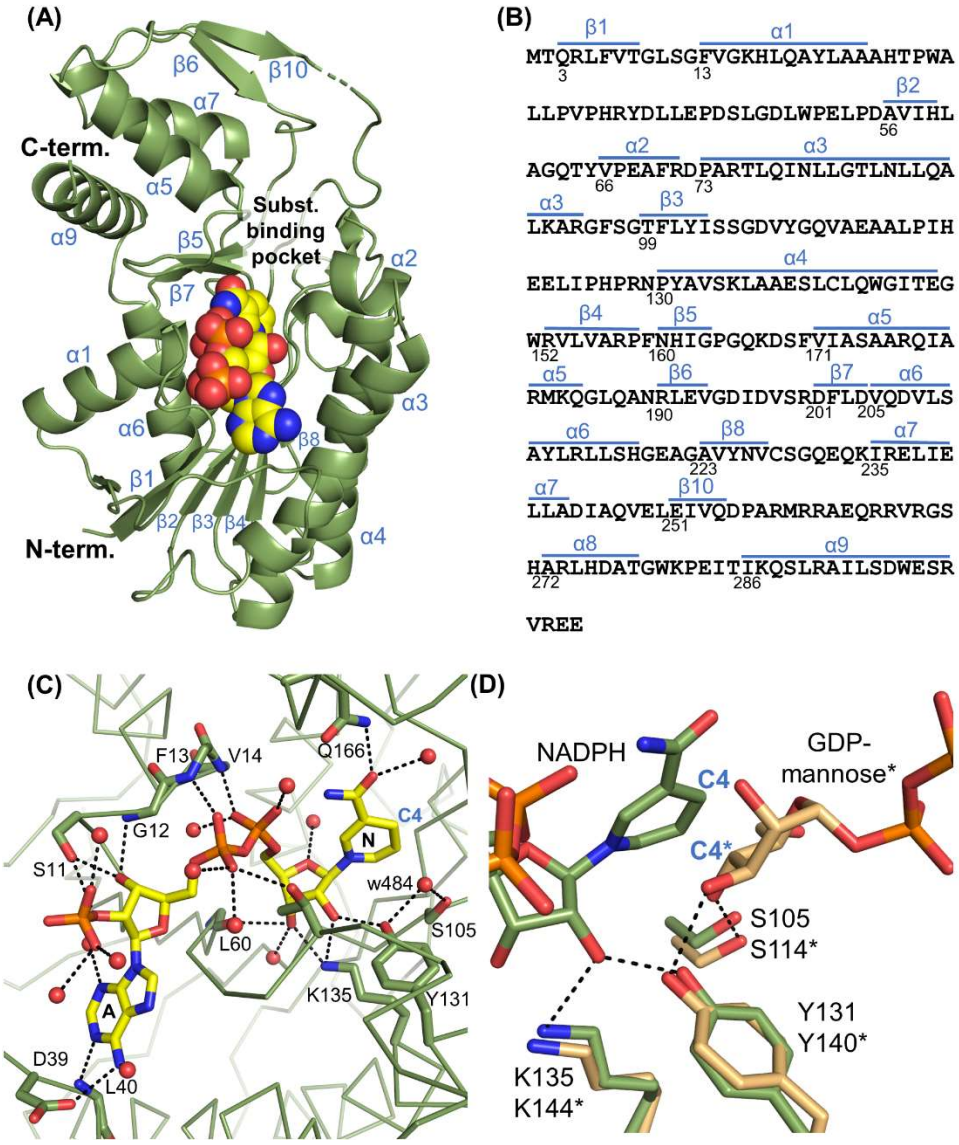

Figure 1

SUPPORTING INFORMATION

GDP-D-rhamnose biosynthesis pathway, additional materials and methods, stereo figures, and RMD catalytic mechanism.